Review of Scientific Instruments

RESEARCH ARTICLE | DECEMBER 18 2023

Tabletop extreme ultraviolet reflectometer for quantitative nanoscale reflectometry, scatterometry, and imaging

Yuka Esashi; Nicholas W. Jenkins; Yunzhe Shao; Justin M. Shaw; Seungbeom Park; Margaret M. Murnane; Henry C. Kapteyn; Michael Tanksalvala

Rev. Sci. Instrum. 94, 123705 (2023)
https://doi.org/10.1063/5.0175860

09 July 2024 17:34:48

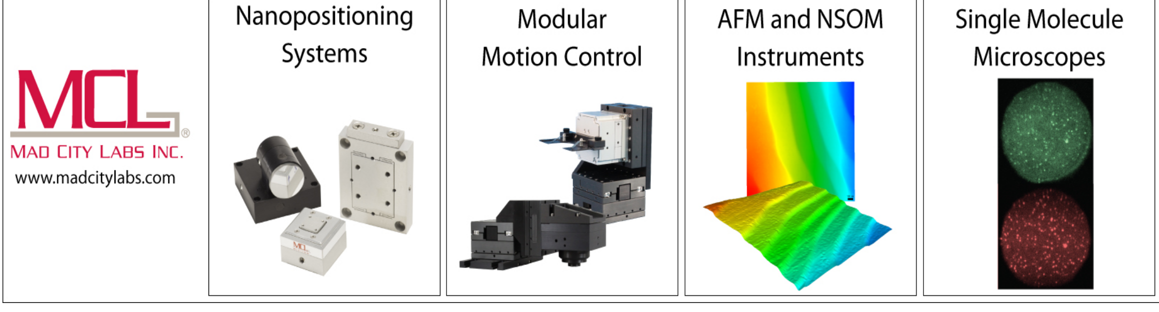

Tabletop extreme ultraviolet reflectometer for quantitative nanoscale reflectometry, scatterometry, and imaging

Cite as: Rev. Sci. Instrum. 94, 123705 (2023); doi: 10.1063/5.0175860
Submitted: 9 September 2023 • Accepted: 18 November 2023 •
Published Online: 18 December 2023

View Online

Export Citation

CrossMark

Yuka Esashi,[1,a)] Nicholas W. Jenkins,[1] Yunzhe Shao,[1] Justin M. Shaw,[2] Seungbeom Park,[3] Margaret M. Murnane,[1] Henry C. Kapteyn,[1,4] and Michael Tanksalvala[1]

AFFILIATIONS

[1] Department of Physics, JILA, and STROBE NSF Science and Technology Center, University of Colorado Boulder and NIST, Boulder, Colorado 80309, USA
[2] Quantum Electromagnetics Division, National Institute of Standards and Technology, Boulder, Colorado 80305, USA
[3] Core Technology R&D Team, Mechatronics Research, Samsung Electronics Co., Ltd., Hwasung 18848, Republic of Korea
[4] KMLabs Inc., Boulder, Colorado 80301, USA

[a)] **Author to whom correspondence should be addressed:** yuka.esashi@colorado.edu

ABSTRACT

Imaging using coherent extreme-ultraviolet (EUV) light provides exceptional capabilities for the characterization of the composition and geometry of nanostructures by probing with high spatial resolution and elemental specificity. We present a multi-modal tabletop EUV imaging reflectometer for high-fidelity metrology of nanostructures. The reflectometer is capable of measurements in three distinct modes: intensity reflectometry, scatterometry, and imaging reflectometry, where each mode addresses different nanostructure characterization challenges. We demonstrate the system's unique ability to quantitatively and non-destructively measure the geometry and composition of nanostructures with tens of square microns field of view and sub-nanometer precision. Parameters such as surface and line edge roughness, density, nanostructure linewidth, and profile, as well as depth-resolved composition, can be quantitatively determined. The results highlight the applicability of EUV metrology to address a wide range of semiconductor and materials science challenges.

Published under an exclusive license by AIP Publishing. https://doi.org/10.1063/5.0175860

I. INTRODUCTION

Advances in next-generation semiconductor and quantum devices can benefit from new nanometrology capabilities that can accurately and non-destructively probe with high spatial resolution.[1,2] Modern devices often rely on intricately designed 3D multilayer structures with layer thicknesses as small as a few nanometers. As device dimensions shrink to the nanoscale, their functional properties can no longer be accurately described by macroscopic models due to the increasing impact of imperfections—such as interface roughness and oxide layers—on their properties and performance.[3–5] While precise control over the geometry and composition of these structures is crucial for device function, non-destructive characterization poses a great challenge.

Common techniques for measuring the geometry and composition of fabricated nanostructures include scanning electron microscopy (SEM), optical and x-ray reflectometry and scatterometry, ellipsometry, atomic force microscopy (AFM), and scanning transmission electron microscopy (STEM). These techniques have sensitivity to different quantities, and it is often the case that no single metrology technique is comprehensive enough to capture all the relevant parameters of a sample. Moreover, the diverse requirements posed by different samples and applications, such as field of view, spatial resolution, elemental and chemical contrast, throughput, ease of sample preparation, and non-contact or non-destructive modes of operation, cannot be fulfilled by a single technique. In pursuing holistic approaches to metrology where combinations of multiple techniques are used to characterize a sample, it is desirable to have a wide range of techniques with different capabilities.

Here, we present a multi-modal extreme ultraviolet (EUV) reflectometer with unique capabilities. This system enables quantitative, non-destructive, and spatially resolved extraction of nano-

09 July 2024 17:34:48

structure geometry and composition with minimal or no sample preparation. It can probe large areas, achieve angstrom-level sensitivity to topography, and provide good elemental contrast. This EUV reflectometer can be used in three distinct modes, with each addressing distinct length scales and periodicity of nanostructures. The first mode is intensity reflectometry, where the specular reflectivity of a transversely uniform sample is measured as a function of the incidence angle. This mode is useful for assessing layer thicknesses, surface/interface roughness, and the composition of bulk or multilayered samples.[6–15] The second mode is scatterometry, where the diffraction efficiency of periodic structures is measured as a function of the incidence angle. This mode allows for precise determination of the geometry and material parameters of periodic nanostructures.[16–24] The third mode, which is the most versatile, complex, and unique mode of this system, is imaging reflectometry.[25] In this mode, diffraction data are used to reconstruct high-resolution phase-and-amplitude reflectivity images of a sample at multiple incidence angles using coherent diffractive imaging (CDI). This mode is suitable for evaluating complex, non-periodic structures.

EUV light offers exceptional capabilities for compositional characterization, owing to its large interaction cross section over a wide range of materials as well as its high elemental specificity due to the presence of element-specific absorption edges in this wavelength range. Moreover, except near the characteristic core-level absorption edges in materials, EUV photons primarily coherently scatter off core electrons and are not influenced by electrons that participate in chemical bonding. This allows for the *ab initio* calculation of optical constants for arbitrary materials using tabulated elemental scattering factors and the number density of each elemental species. In contrast, optical constants in the visible, vacuum ultraviolet (VUV), and infrared (IR) spectral regions are sensitive to chemical bonds and usually require experimental measurements at specific wavelengths for each material, even for a minor change in chemical composition. Regarding dimensional measurements, the short wavelength of EUV light (~10–100 nm) enables high-resolution imaging at

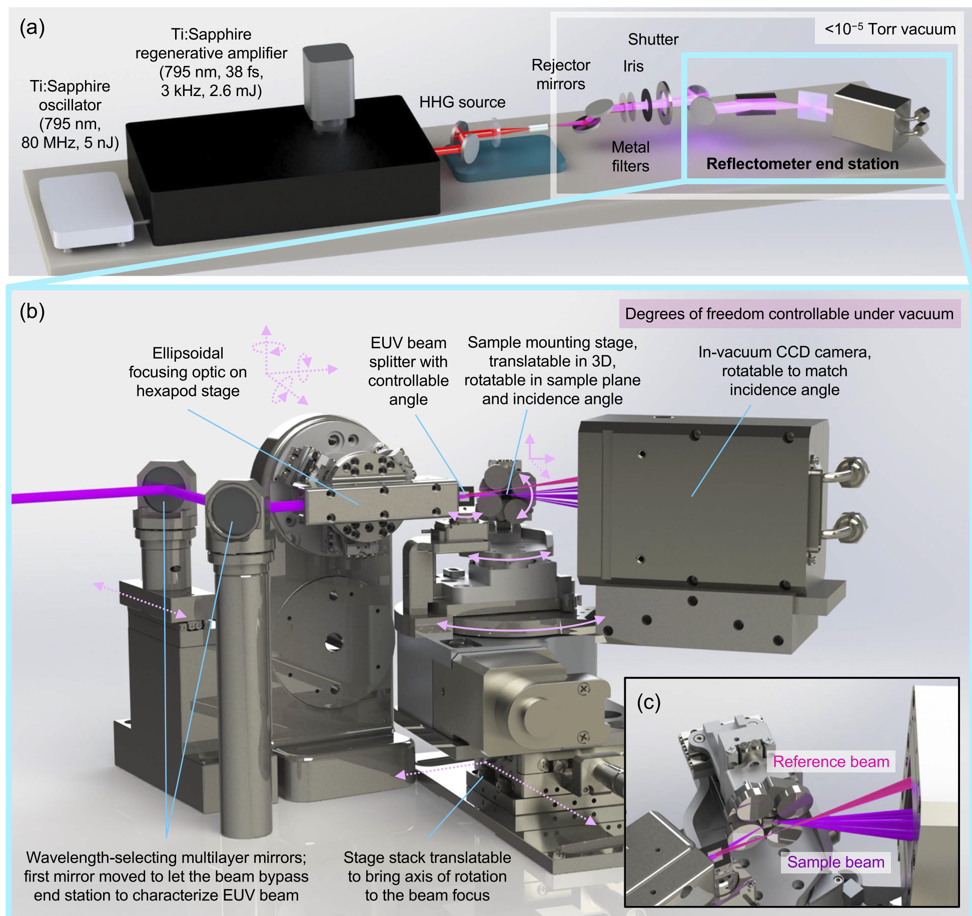

FIG. 1. Multi-modal extreme ultraviolet tabletop reflectometer setup. (a) Schematic of the entire beam line. (b) Schematic of the reflectometer. Degrees of freedom that are controllable under vacuum are indicated by pink arrows; stages indicated by solid-line arrows are primarily used during data collection, while ones indicated by dotted-line arrows are primarily only used for alignment. (c) Zoom-in from a different angle, showing that the reflected beam from the beam splitter is directed straight to the camera to act as a reference beam; the transmitted beam reflects from the sample.

09 July 2024 17:34:48

Published under an exclusive license by AIP Publishing

the diffraction limit, as well as enhanced sensitivity to interfaces and small topographic deviations. Furthermore, EUV light exhibits a favorable combination of penetration depth and reflectivity: it can penetrate several tens to hundreds of nanometers into materials that are opaque to visible light, making it possible to access buried interfaces. EUV light also has a high reflectivity even at incidence angles of tens of degrees from grazing, allowing the incident beam to remain small without suffering from the projection effects encountered by x-ray reflectometers that operate at extreme grazing angles.[26–29] Finally, the ability to generate bright and coherent EUV light using high harmonic generation (HHG) tabletop sources presents an exciting opportunity for the development of new and compact nano-characterization tools.

II. EXPERIMENTAL SETUP

Figure 1(a) shows the experiment layout for the tabletop EUV reflectometer beamline. A modelocked Ti:sapphire laser of center wavelength λ = 795 nm, 80 MHz repetition rate, and 5 nJ pulse energy seeds a Ti:Sapphire regenerative amplifier (KMLabs Wyvern HP). The amplifier provides 38 fs pulses at a 3 kHz repetition rate, with pulse energy up to 2.6 mJ. To reduce the detrimental nonlinear B-integral associated with a high peak laser intensity, we use a fraction (<1 mJ) of the laser energy and propagate it through the beamline as a chirped pulse. The pulse is then compressed using a sequence of chirped mirrors immediately prior to the high harmonic EUV generation step. This approach works well for high harmonic wavelengths of ~30 nm that do not require high laser pulse intensity. The pointing of the driving laser is controlled using a pair of cameras and piezo-actuated mirrors that stabilize the beam centroid at two points along its propagation.

The beam is focused into either a hollow-core waveguide or a semi-infinite gas cell (modified prototype KMLabs XUUS4) to generate coherent extreme ultraviolet light via HHG around photon energies of ~41.5 eV. The rest of the beamline is kept at a vacuum of $<10^{-5}$ Torr to prevent absorption of the EUV light in air. The EUV source is detailed further in Sec. III.

Several optics are used prior to the reflectometer to separate the EUV beam from the driving IR beam. Two rejector mirrors (Gooch & Housego) used near the Brewster angle of the IR light reflect the EUV while absorbing much of the driving laser. A plasma cleaner (PIE Scientific EM-KLEEN) positioned above the first rejector mitigates hydrocarbon contamination. The plasma cleaner is typically run with a 20%–80% mixture of O_2 and Ar for optimal cleaning. The rejectors are followed by up to two metal foil filters (Luxel) that further attenuate the IR intensity to significantly below the noise floor. The filters can be swapped or removed without breaking the vacuum. An adjustable iris sets the on-camera mode shape of the EUV. A shutter (Uniblitz VS14S2T0-EC2) is synchronized to the camera exposures to prevent streaking during camera readout.

Figure 1(b) shows the reflectometer setup and the mechanical degrees of freedom that are controllable under vacuum. First, the EUV beam is incident onto two 45° angle-of-incidence multilayer mirrors (NTT Advanced Technology Corporation) that allow for alignment of the beam into the reflectometer setup and the final selection of the EUV wavelength from the comb of harmonic frequencies generated by HHG. The EUV beam is then focused by a custom ellipsoidal optic (machined by Welch Mechanical Design), consisting of an 80 nm Ni coating on an Al substrate, designed for a 5-degree angle-of-incidence. The ellipsoid focuses the beam onto the sample, with a demagnification of 22×, to a spot of ~3 μm diameter. (The EUV focus size can be measured by moving a sharp edge of a sample across the beam to perform a knife-edge test and confirmed by computational imaging reconstructions of the beam; see Sec. V C and Fig. S1 in the supplementary material.) Since the beam is oriented near grazing incidence with respect to the sample, the beam elongates, and its width in the horizontal direction increases by up to 5.8× at 10° from grazing. The ellipsoidal optic is mounted on a hexapod (Smaract SmarPod 70.42-HV) that allows rotation and translation around three axes for precise alignment. The incident beam on the sample is S-polarized. The beam divergence half-angle at the sample is roughly 0.5°, depending on how tightly the iris is closed. Note that the first EUV multilayer mirror can be translated out of the EUV beam, which then bypasses the reflectometer and instead is incident onto a diagnostic camera for viewing the direct, unfocused beam.

Immediately following the ellipsoid is a removable 50 nm thick Si membrane (Norcada NSUF1065A) coated with 3 nm of Pt on a rotation stage (Smaract SR-2013). This is used as an EUV beam splitter to generate a reference beam that is directed to the edge of the camera for reflectometry measurements that greatly benefit from EUV beam intensity normalization. The transmitted EUV beam is focused on the sample, and the specular reflected beam from the sample is directed to the center of the camera sensor. This geometry is shown in Fig. 1(c). The Pt coating on the beam splitter membrane serves a dual purpose: first, it helps to balance the reflected and transmitted power from the beam splitter (~5% and ~13%, respectively; the transmitted arm is set higher to account for the further reduction from the reflection on the sample). Second, it minimizes the sensitivity of the reflectivity to small variations in wavelength and incidence angle, which would otherwise introduce noise into the reference measurement. The power ratio can further be optimized by adjusting the rotation of the beam splitter. For measurements that do not benefit from a reference, the beam splitter can be rotated out of the beam path.

The sample is mounted on a customized stack of stages that allows for 3D linear translation (three Smaract SLC-1730-HV) and sample-plane rotation (SR-2013-S-HV) for navigation, orientation, and scanning, as well as rotation around the vertical axis (SR-2812-S-HV) to change the incidence angle of the EUV beam. A total of five modified SEM stubs can be loaded for sample mounting, and samples of thickness up to ~2 mm are accommodated. The sample-mounting stage can be positioned with the sample face parallel to the illumination and can be retracted away from the beam path, enabling the beam to propagate freely to the detector. This is useful for determining the intensity of the incident beam on the sample as well as for measuring the out-of-focus beam mode.

The in-vacuum CCD EUV camera (Princeton Instruments MTE2 used for these measurements) is mounted on a rotation stage (Newmark RM-3-101V–C1) and is designed to rotate with the sample in a θ–2θ configuration to maintain the EUV light on the camera as the sample is rotated. The camera uses a flexible readout cable and cooling water line bellows to allow for smooth movement inside the chamber. The vertical rotation axes of the camera and the sample are aligned to each other using a positive stop. These axes of rotation are mounted together on two linear stages (OptoSigma TSDS-652CUU),

09 July 2024 17:34:48

Published under an exclusive license by AIP Publishing

which are used to align the rotation axes with the beam focus. The surface of the sample is brought to the rotation axes by inserting one of the 3D linear translation stages, which is necessary to maintain the beam's position on the sample as the incidence angle is changed.

The camera is configured such that 200 light-insensitive overscan columns are read out with each frame. The pixels in these columns serve to characterize several independent sources of background or noise on the detector, such as the standard deviation of the readout noise and the analog-to-digital converter (ADC) offset. These statistics can be used to minimize the effect of noise between frames or even within a single frame.

The stage stack can perform reflectometry over a range of 0–55° from grazing while keeping the diffraction on the camera sensor. If moving this full range, the sensor can be as close to the sample as 30 mm, corresponding to 0.42 NA and a diffraction limited resolution in the vertical direction of ~36 nm when using 30 nm illumination (or ~16 nm when using 13 nm illumination). Due to conical diffraction, the resolution in the horizontal direction suffers by a factor of ~$1/\sin(\theta)$, where θ is the incidence angle measured from grazing. As discussed in the later sections, the axial precision is on the order of an angstrom, depending on the sample and the amount of data collected.

The material of the rejector optics, metal filters, and multilayer mirrors employed in the beamline depends on the target EUV wavelength. For 30 nm, Si rejectors, Al filters, and SiC/Mg multilayer mirrors are used. For 13 nm, Ru-coated Si rejectors, Zr filters, and Mo/Si multilayer mirrors are used.

The experimental software for this system allows automatic and programmed movement of the sample and the camera for data collection. Importantly, when the sample is rotated to change the incidence angle of the beam, a slight misalignment between the beam focus, the sample rotation axis, and the sample surface can cause the beam spot to translate horizontally on the sample. The software allows for a calibrated correction of this offset such that it is possible to stay on the same field of view as data are collected across a range of incidence angles. The software also allows the user to set different exposure times for data frames collected at different incidence angles to maximize the use of the camera's dynamic range despite the change in reflectivity as a function of the incidence angle. At a single beam position on the sample, duplicate frames with varied exposure times can also be collected and subsequently combined for higher dynamic range data. Finally, the order in which incidence angles are addressed is randomized to decouple any systematic error from the resultant curve.

III. HIGH-HARMONIC GENERATION EUV LIGHT SOURCE

The high-harmonic generation setup consists of either a 150 μm inner diameter hollow-core fiber or a semi-infinite gas cell (sealed with a blank metal Swagelok VCR gasket) that is optimized to produce a comb of discrete frequencies around 30 nm. To generate 30 nm of light, the fiber/gas cell is filled with ~30 Torr of Ar gas, and the pulse energy is set to roughly 0.83 mJ at the input of the fiber/gas cell. In this case, harmonics between 27 and 38 nm are generated. Although it is possible to use this same setup to generate 13 nm light (harmonics between 11 and 16 nm), the laser delivery optics and gas handling systems were not optimized for the high gas pressures (~600 Torr of He gas) and high laser pulse energies (~2.7 mJ pulses) required.

The total EUV flux integrated over the harmonic comb is on the order of 10^{12} photons/sec at the source using Ar gas, with the flux limited by the 3 kHz repetition rate of the driving laser (using a higher repetition rate laser and a more optimal geometry, the EUV flux can be further enhanced by ~100×; however, the throughput of the system would still be limited by the CCD camera readout rate). From this beam, the incident flux on the sample is roughly 10^9 photons/sec in a single harmonic order at 30 nm due to optic loss and narrowed bandwidth. For example, assuming minimal surface roughness and no surface contamination, the reflectivity for 30 nm light from a single rejector or a multilayer mirror is ~0.5, that of the ellipsoid is ~0.8, and the transmission of a single 0.2 μm Al filter is ~0.4.

We tested the stability of the source over 30 minutes by first using a photodiode to monitor the pulse-to-pulse IR laser intensity as well as the second harmonic (generated by passing the IR laser beam through a beta barium borate crystal). The EUV intensity and pointing stability were then measured after propagating the HHG beam 2.5 m from the source onto a CCD camera with a 10 ms exposure time. The EUV spectrum was also measured using a diagnostic beamline consisting of a toroidal focusing optic and a grating. The IR, the second harmonic, and the EUV intensity rms stabilities were 0.85%, 1.7%, and 1.36%, respectively. The unfocused EUV beam had an rms pointing stability of 15 μrad, corresponding to <1% of the beam radius, while the spectrum had an rms energy stability of 22 meV for the 27th harmonic at around 30 nm.

We also verified the harmonic selectivity of the system by inserting a grating as the sample and collecting the diffraction orders on the CCD camera. Not accounting for the slight wavelength-dependence of the diffraction efficiency, we found the 25th, 23rd, and 21st orders to have 4%, 0.6%, and 0.07% of the intensity of the 27th harmonic.

IV. SAMPLE MODELING AND DATA FITTING PROCEDURES

All three modes of reflectometry that the system offers involve the inverse problem of finding a sample model with a theoretically calculated signal that matches the experimentally measured signal.

To calculate the expected reflectivity or diffraction efficiency for a given sample, it is first necessary to determine the index of refraction of the constituent materials assumed by the model at the illumination wavelength. The light–matter interaction of EUV photons is dominated by core electrons; thus, the index of refraction n depends only on the number density of each elemental species and can be calculated using pre-characterized elemental scattering factors in the following equation:[30]

$$n = 1 - \delta - i\beta = 1 - \frac{r_e}{2\pi}\lambda^2 \sum_j n_j (f_{1,j} + i f_{2,j}). \quad (1)$$

In the x-ray and EUV regimes, the index is very close to 1, and so it is often expressed using $\delta, \beta \ll 1$. Note that the sign on β can change depending on the sign convention used to describe electromagnetic

09 July 2024 17:34:48

Published under an exclusive license by AIP Publishing

plane waves. r_e is the classical electron radius, λ is the wavelength of the light in vacuum, n_j is the number of atoms of type j per unit volume, and $f_{1,j}$ and $f_{2,j}$ are the real and imaginary parts of the unitless atomic scattering factor for that atom type. Scattering factors are tabulated in multiple databases;[31,32] in this paper, we use the database from the Center for X-ray Optics (CXRO).[31]

Second, the index of refraction is used in Parratt formalism[33] calculations to predict the complex reflectivity from a transversely uniform region or a large structure (i.e., with a width many times the wavelength). Parratt formalism uses Fresnel coefficients at each interface in a recursive computation to rigorously calculate both the amplitude and phase of the reflected (or transmitted) wave as it hits a multilayered stack for a given incidence angle and wavelength. This formalism also allows the use of Névot–Croce factors to approximate the effect of surface and interface roughness on reflectivity.[34,35]

Reflectivity calculated by Parratt formalism can be combined with Fourier optics to obtain the diffraction efficiency of periodic structures that are wide and thin relative to the wavelength. In doing so, it is important to account for the geometric phase shift that arises from surface topography. This can either be incorporated into the Parratt calculation by placing a layer on top of the recessed parts of the sample with the vacuum index or by adding the following geometric phase shift φ:

$$\varphi = 360^\circ[2h \sin(\theta)/\lambda], \tag{2}$$

where h is the recessed height, θ is the incidence angle measured from grazing, and λ is the wavelength of the light in the external medium.

While this was not used for the demonstrations in this publication, for sub-wavelength and/or higher aspect-ratio structures where 3D effects of diffraction become more prominent, electromagnetic solvers such as Rigorous Coupled-Wave Analysis (RCWA)[36,37] should be used at the expense of increased computation time.

Third, to optimize the sample model to fit the experimental data, the sample model must be parameterized in terms of material, layer thicknesses, and surface/interface roughness. Out of all the parameters, some are chosen as parameters of interest to be solved, while others are fixed at their nominal or measured values. In addition to the sample parameters, we self-calibrate our system by fitting for small offsets in the wavelength and sample incidence angle to account for slight misalignments. In addition, we sometimes also solve for the deposition rate of carbon contamination due to EUV-induced dissociation of hydrocarbons. This is solved as a scaling of the cumulative fluence on the sample, which is the dominant factor that determines the carbon deposition rate.[38]

Fourth, we use a multi-variable optimization scheme to fit the model to the data. While there are many available, we use the genetic algorithm, which is an optimization method that is based on natural selection, with Matlab's *ga*() function. The genetic algorithm has been shown to work well with X-ray Reflectivity (XRR) measurements due to their robustness and ability to find the global minimum when many local minima are present.[39,40] The algorithm can also be run multiple times with different sets of initial populations to verify that the found solution is the global minimum.

The error metric that is minimized in the genetic algorithm is the chi-square, χ^2,[41]

$$\chi^2 = \sum_{i=1}^{N} \left(\frac{y_i - y(\theta_i|\boldsymbol{a})}{\sigma_i} \right)^2, \tag{3}$$

where the summation is over N data points. y_i is the measured data, $y(\theta_i|\boldsymbol{a})$ is the theoretically calculated datapoint for incidence angle θ_i and the vector of solved-for parameters $\boldsymbol{a}$, and σ_i is the standard error of the mean for that data point.

Finally, once a good fit to the data have been found, the error bars of the solved parameters can be calculated using the covariance matrix;[41] this procedure is outlined in the supplementary material. While the error bars reported from the covariance matrix take account of the correlation between the parameters (hence we refer to this as the "multi-parameter" confidence interval), it is also possible to calculate a "single-parameter" confidence interval by individually varying parameters in the solution until the χ^2 error metric increases by $\Delta\chi^2$. This is a rough estimate of how low the confidence intervals could be if more parameters were fixed, meaning less parameters are jointly solved for. It is intended to give an idea of the order-of-magnitude sensitivity of 30 nm light to each parameter. For the demonstrations in this paper, both of these confidence intervals are reported for 1σ (i.e., $\Delta\chi^2 = 1$).

V. THREE MODES OF REFLECTOMETRY

A. Intensity reflectometry

In intensity reflectometry mode, we measure the specular reflectivity of the EUV beam on the sample as a function of incidence angle to solve for layer thicknesses, surface and interface roughness, and other material parameters on transversely uniform sample surfaces. EUV intensity reflectometers have been demonstrated for the characterization of EUV optical constants and multilayer optics, both at synchrotrons[6–10] and on table-top systems.[11–15]

In this mode, four types of data are collected. The first type are the "sample" frames that measure the beam reflecting from the sample at each incidence angle. In these frames, the reference beam that is split off from the beam splitter is also captured simultaneously. The second type are the "beam" frames, where the sample is translated out of the way of the beam to allow it to go directly onto the camera at normal incidence. These frames serve to measure the absolute flux of the EUV beam. The third and fourth types are the background frames for both the sample and the beam frames, which are collected with the shutter closed so that no EUV photons reach the detector. The collected data are processed (procedure detailed in the supplementary material) to obtain the absolute reflectivity as a function of angle.

To demonstrate the intensity reflectometry mode, the reflectivity of a 100 nm thick Au film deposited on a Si substrate was measured. Intensity reflectometry mode can utilize the optional EUV beam splitter for normalization of the incident intensity, so first, to characterize the performance of the beam splitter, 400 sample frames were collected at 30° from grazing. All frames (for the beam splitter characterization and the actual reflectometry) were collected at the 2 MHz readout rate of the CCD cooled to 10 °C. While the camera can be cooled down to a lower temperature, we only cool it down to a temperature that is necessary to sufficiently

09 July 2024 17:34:48

Published under an exclusive license by AIP Publishing

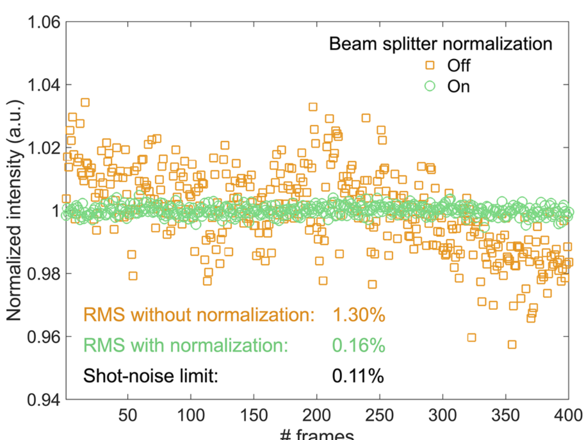

FIG. 2. Intensity normalization using the EUV beam splitter. Normalized intensity of the EUV beam reflecting off the Au thin film sample as a function of camera frames, with and without normalization using the EUV beam splitter. Fluctuations are greatly reduced to a level close to the shot-noise limit. Each frame collects ~1.5×10^6 photons in the beam reflecting off the sample.

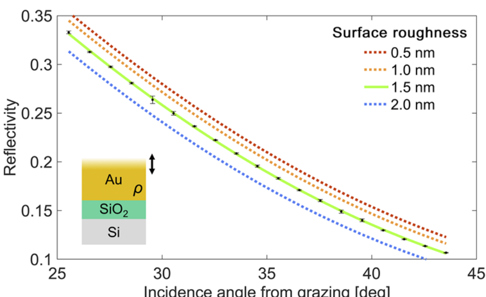

FIG. 3. Intensity reflectometry on a 100 nm Au thin film on a Si substrate to determine the surface roughness and density. The measured reflectivity (black datapoints with error bars) and the theoretical solution fit (solid light green) with a surface roughness value of 1.5 nm. Additional theoretical curves calculated from the found solution with varied surface roughness are also shown in dotted lines. Inset: cross-sectional sample schematic and solved parameters.

mitigate noise while minimizing condensation of moisture on the camera sensor from the imperfect vacuum.

Figure 2 shows the intensity of the beam reflecting from the sample, measured in the 400 frames collected at 30°, with and without beam splitter intensity normalization. With a 0.18 s exposure time, each frame collects ~1.5×10^6 photons. The rms of the per-frame intensity is reduced from 1.30% to 0.16% via normalization, and this stability is very close to the shot-noise limit of 0.11% for the photon flux in this experiment.

For the actual intensity reflectometry on the gold film sample, 50 frames of "sample" data were collected at 19 angles between 26 and 44° from grazing in 1° increments, at an exposure time of 0.22 s. At each angle, over the course of collecting the frames, the sample was translated vertically by 735 μm (15 μm per frame) to ensure that the reflectivity measured at one angle is the average across an area and is not negatively influenced by small defects that might be present on the sample; this translation can be decreased or eliminated to measure an area as small as a few μm^2 if desired. Ten frames of "beam" data were collected in between each group of "sample" frames at an exposure time of 0.13 s. For each group of "sample" or "beam" frames, three background frames were collected.

Figure 3 shows the measured reflectivity from the gold thin film sample as a function of the incidence angle. The use of the beam splitter normalizes out the incident beam power fluctuation, resulting in small error bars of ~0.1%. The model of the sample was parameterized by the surface roughness and the density of the gold film (the model of this and other samples that were used in this publication is detailed in the supplementary material). The fitted model parameters found using the genetic algorithm are shown in Table I. While the multi-parameter confidence interval on the Au density is relatively large, the surface roughness is solved to a sub-nanometer confidence interval. This sensitivity is also shown by the <1 Å single-parameter confidence interval, as well as the well-separated theoretical curves in Fig. 3 that are calculated using the

TABLE I. Fitted surface roughness and density with confidence intervals of the Au thin film sample measured by intensity reflectometry.

	Fitted parameters	Confidence interval	
		Multi-parameter	Single-parameter
Surface roughness (nm)	1.5	0.9	<0.1
Au density (g/cm^3)	18.5	3.0	0.01

09 July 2024 17:34:48

solution but with different surface roughness. The fitted parameters are consistent with the surface roughness that was measured on an AFM (1–1.5 nm), optical profilometer (0.8–1.5 nm), and XRR (~1.7 nm), the density measured by XRR (18.5–19.1 g/cm^3), and the expected density of Au in a thin-film (18.4–19.2 g/cm[42,43]). Slight discrepancies are deemed reasonable, as each technique measured a slightly different location and field of view on the sample at different spatial resolutions.

B. Scatterometry

EUV scatterometers for the characterization of nanoscale gratings have been developed in several different configurations;[16–24] diffraction efficiency can be measured at one or many wavelengths, at only some or many diffracted orders. In our system, we measure the diffraction efficiency in multiple diffracted orders using a single wavelength as a function of the incidence angle.

The collected data and the analysis procedure are similar to the intensity reflectometry mode. We collect "sample" data that captures the diffraction pattern as well as the associated background frames. It is possible to interleave direct beam image frames with sample scattering frames to monitor the beam power; however, this is not critical for this mode since the diffraction efficiency is calculated as a ratio between the different orders of the diffraction, making it insensitive to power fluctuations.

Published under an exclusive license by AIP Publishing

The data are processed as outlined in the supplementary material to obtain the frame-by-frame counts in each of the diffraction orders at each incidence angle. Then, diffraction efficiency for $\pm m$th order D_m is calculated using the following equation:

$$D_m = \text{mean}\left(\frac{C_{+m} + C_{-m}}{C_{+m} + C_{-m} + C_0}\right), \quad (4)$$

where C_m is the counts recorded in the mth order in a single frame, and the mean is taken across multiple frames collected at a given incidence angle.

To demonstrate this mode, we measured Ni line gratings with a nominal 100 nm linewidth, 400 nm period, and 12.9 nm height patterned using electron lithography on a polished sapphire substrate. 50 frames of grating diffraction were measured at 30 angles between 11 and 40° from grazing in a 1° increment at varying exposure times between 0.23 and 8.5 s, depending on the incidence angle. At each angle, over the course of collecting the frames, the sample was translated vertically by 98 μm (2 μm per frame). Three background frames were also collected at each angle. The grating was oriented with grating lines parallel to the plane of incidence of the EUV beam (conical mounting). All frames were collected at the 2 MHz readout rate of the CCD cooled to 10 °C.

While this sample was designed for a rectangular cross-sectional profile, the AFM image as shown in Fig. 4(b) revealed that the fabricated structures deviated in two important ways: first, there is a significant line edge roughness (LER) to the lines of the grating, and second, there is a pedestal of several nanometers at the base of the grating.

The AFM imaging of the sample was motivated by the fact that it was not possible to fit the diffraction efficiency of all first, second, and third orders with a simple grating model of a rectangular cross section, as shown in Fig. 4(c). As shown in Figs. 4(d) and 4(e), the introduction of only the LER or the pedestal in the sample model was able to improve the fit significantly, but the genetic algorithm still did not find a set of parameters that fit all three diffraction efficiency curves. As shown in Fig. 4(f), only when both the LER and the pedestal were introduced was it possible to fit all three curves.

LER was modeled using a Debye–Waller-like factor that approximates the effect of LER as a damping of the scattered intensity,[44,45]

$$I_{DWF}(q_y) = I_0(q_y)\exp\left(-\xi^2 {q_y}^2\right), \quad (5)$$

where I_{DWF} and I_0 are the intensity of the diffraction orders of gratings with and without LER, respectively, $q_y = (2\pi m/\text{grating period})$, and m is the order of diffraction. ξ is the standard deviation of the grating edge displacement. The applicability of this factor for EUV scatterometry has been demonstrated, as long as the grating edge displacement follows a normal distribution and when ${q_y}^2\xi^2 \ll 1$.[22] For the grating under consideration, which is thin relative to the wavelength, this formulation of LER can be incorporated into the Fourier optics calculation of diffraction efficiency.

In the final fit shown in Fig. 4(f), the solved parameters were the width of the tall main part of the grating, the main grating LER, and the width and height of the pedestal. These parameters are illustrated in Fig. 4(a). The solved parameter values and their confidence intervals are reported in Table II. The AFM measured a main grating width of 56–80 nm, an LER of 5.6–6.5 nm, a pedestal width of 100–140 nm, and a pedestal height of 4–6 nm. In general, some discrepancy between EUV scatterometry and AFM measurements is to be expected since the AFM measures over a much smaller area of the grating. The discrepancy between EUV scatterometry and AFM in LER is likely due to the finite tip size of the AFM (1–2 nm radius of curvature), making it insensitive to high frequency components of the LER, and because AFM measures a top-down picture of the gratings while EUV scatterometry

09 July 2024 17:34:48

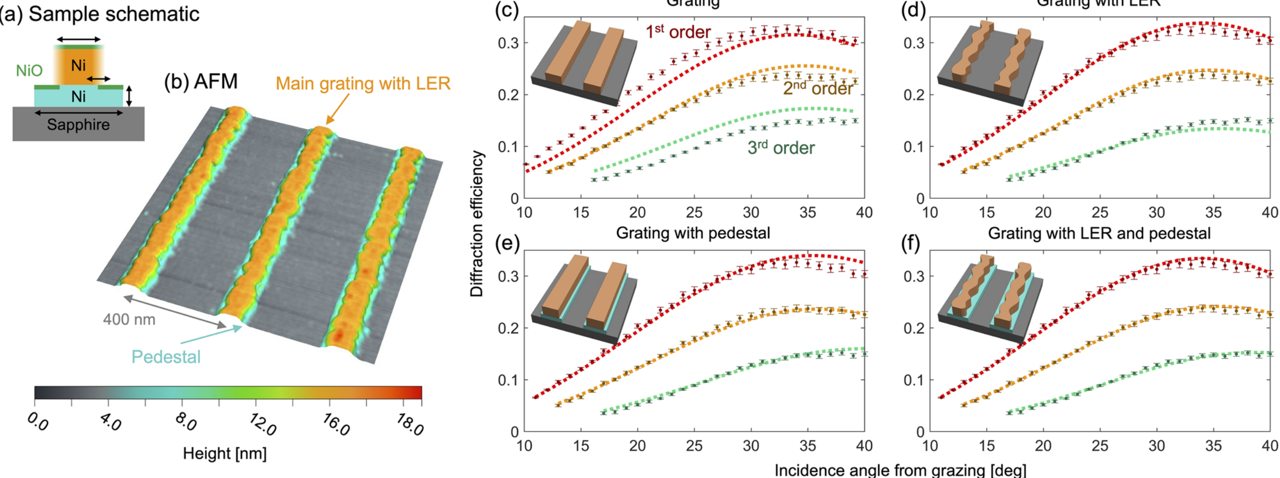

FIG. 4. Scatterometry of Ni line gratings on a sapphire substrate to measure the grating profile. (a) Cross-sectional sample schematic and solved parameters. (b) Atomic force microscopy image of the sample. (c)–(f) Measured first, second, and third order EUV diffraction efficiency as a function of the incidence angle and best fits obtained for (c) simple rectangular grating, (d) grating with line edge roughness (LER), (e) grating with a pedestal, and (f) grating with LER and a pedestal. The best agreement with the data are for a model that includes both LER and a pedestal.

Published under an exclusive license by AIP Publishing

TABLE II. Fitted parameters and confidence intervals for the linewidth, LER, and pedestal height width and height of the Ni gratings on the sapphire substrate as measured by EUV diffraction scatterometry.

	Fitted parameters	Confidence interval	
		Multi-parameter	Single-parameter
Main grating width (nm)	64.7	0.8	0.1
LER (nm)	10.0	0.5	0.1
Pedestal width (nm)	151	8	1.6
Pedestal height (nm)	1.2	0.3	<0.1

measures over the height of the grating .[45] The discrepancy in the pedestal height could also partially be due to any remaining subtle differences between the physical sample and the model assumed in EUV scatterometry (rectangular cross section, consisting of Ni, with the same NiO thickness and surface roughness as the main grating). Obtaining a good estimate of absolute parameters using EUV scatterometry relies on accurate modeling of the sample (as with any model-based technique); the single-parameter confidence intervals show a good sensitivity to parameter variations. In comparison with AFM or STEM and similarly to critical-dimension small-angle x-ray scattering (CD-SAXS), the strength of this technique is in the ability to detect spatial variations in sample critical dimensions over large regions in a non-contact, non-destructive mode, with potential applications for in-line inspection or metrology.

The small error bars on the diffraction efficiency are achieved by measuring the ratio of powers in the diffraction orders frame-by-frame, which removes any effect of fluctuation in the incident beam power. The residual variance at each angle comes from sample inhomogeneity; in particular, LER is known not only to decrease the diffraction efficiency but also to increase its variance.[44]

We speculate that the unexpected LER and pedestal structure are due to insufficient optimization of the electron-beam lithography on an insulating substrate, i.e., sapphire. We also note that a precise measurement of LER was challenging on the SEM, again due to the insulating substrate. This necessitated the deposition of a thin discharge layer on top, which decreased the signal level from the Ni grating.

C. Coherent diffractive imaging reflectometry

Ptychography is a coherent diffractive imaging technique that enables precise, quantitative imaging of a sample's complex reflectivity or transmissivity.[46–49] In ptychography, the far-field intensity diffraction patterns are collected as a coherent beam is scanned over overlapping positions on the sample. An iterative phase retrieval algorithm is then used to generate a real-space phase-and-amplitude image of the sample.

Ptychography has found extensive application in the EUV and x-ray wavelength ranges due to its ability to achieve diffraction-limited imaging with high photon-efficiency and without an image-forming lens.[50–53] Ptychography extracts the spatially resolved *complex* (i.e., amplitude *and* phase) reflectivity of an object. In particular, the phase upon reflection exhibits high sensitivity to elemental composition and topography.[25,54] Therefore, by collecting multiple ptychographic images of a sample at different incidence angles, it is possible to perform reflectometry in a spatially resolved manner. We call this technique EUV coherent diffractive imaging reflectometry.[25]

For imaging reflectometry, a ptychographic scan is collected at multiple incidence angles. In addition, beam frames are also collected in between the ptychography scans to monitor the absolute flux of the EUV beam as well as to characterize the propagated beam profile, which can be used in the ptychography algorithm as a constraint.[55] As before, background frames are collected for each ptychography scan and each set of beam frames. The pre-processing steps of the raw data are detailed in the supplementary material.

To reconstruct the images, here we used the mPIE algorithm,[56] although the technique does not depend on the use of any specific implementation of ptychography. It is often helpful to reconstruct images using two mutually-incoherent modes[57,58] to reduce the effects of model mismatch and noise on the main reconstruction.[54] The processed beam data can be used for modulus enforced probe (MEP) constraints[55] that can assist in the convergence of the reconstructed beam probe. In addition, in the case of a piecewise flat sample (as is the case for most lithographically fabricated samples), denoising schemes such as total variation regularization[25,59] can be incorporated into the ptychography loop to improve the image further. The detailed reconstruction procedure for this demonstration is included in the supplementary material.

The reconstructed images are registered to each other, and the phase step between two separate regions of the sample is calculated as a function of the incidence angle (the image analysis procedure is detailed in the supplementary material). While imaging reflectometry theoretically allows the analysis of both the amplitude and phase of the ptychographic images, typically we only look at the phase as it is often reconstructed with higher fidelity. Note that since the phase is only meaningful as a relative measurement, two distinct regions from the images must be chosen to measure the phase step.

We performed imaging reflectometry on a calibrated AFM test sample from BudgetSensors (CS-20NG-UM) that consists of SiO_2 structures on a Si substrate, as shown in Fig. 5(a). A total of 11 ptychographic images were collected between 19° and 29° from grazing in a 1° increment. The distance between the beam focus on the sample and the camera sensor was set to 45 mm, giving an image pixel size of 61 nm (height) by 192 nm (width). At each incidence angle, a ptychographic scan was collected in a 15 × 10 rectilinear grid of 0.35 and 0.6 μm step sizes, at exposure times ranging between 0.4 and 1.0 s. In between the ptychographic scans, ten beam frames were collected. For each ptychographic scan and beam data, three background frames were collected. All frames were collected at the 1 MHz readout rate of the camera, which was cooled to −10 °C. The ptychographic reconstruction procedure is detailed in the supplementary material.

Figure 5(b) shows a full, complex ptychographic reconstruction of the sample. The wide field of view compared to the scan area covered by the $1/e^2$ extent of the probe (roughly indicated by the white dotted square) is an advantage of grazing-incidence reflection-mode ptychography.[25,60] The high-fidelity center regions from all 11 reconstructions are shown in Fig. 5(c), and the corresponding reconstructed probes are shown in the supplementary material. The

09 July 2024 17:34:48

Published under an exclusive license by AIP Publishing

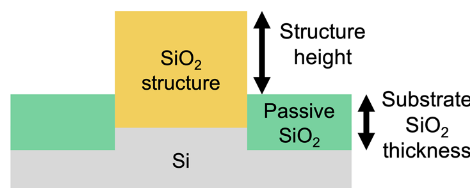

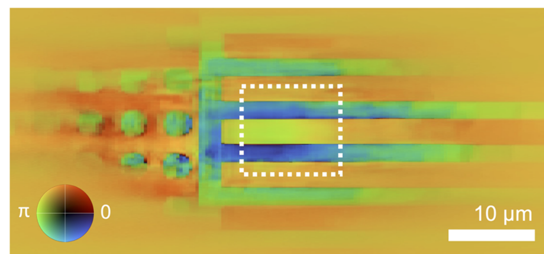

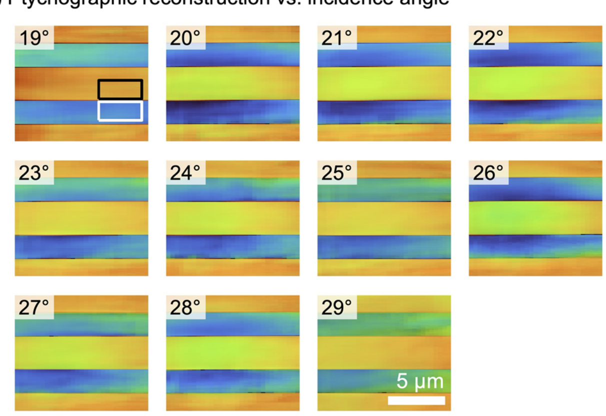

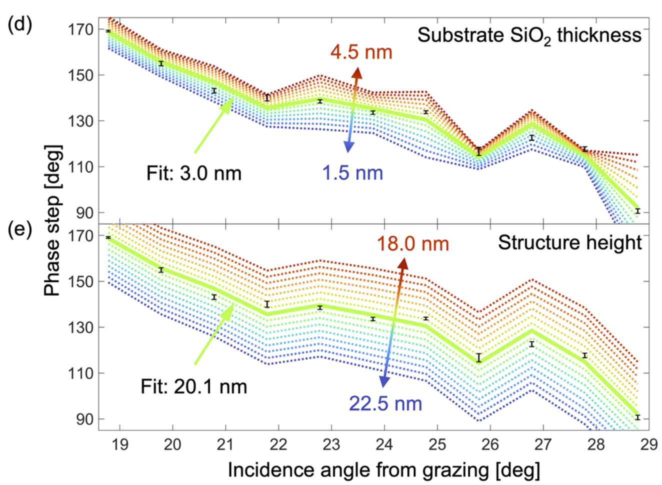

FIG. 5. Imaging reflectometry on SiO_2 structures on a Si substrate to measure substrate SiO_2 thickness and structure height. (a) Sample schematic and the measured parameters. (b) Ptychographic reconstruction at 24° from grazing; brightness corresponds to the amplitude and the hue of the phase, as indicated by the color wheel, which is shared with (c). The white dotted rectangle indicates the cropped region for (c) and corresponds roughly to the area covered by the $1/e^2$ extent of the beam. (c) Center of the ptychographic reconstructions taken at 11 incidence angles. The black and white rectangles shown in the 19° reconstruction indicate the pixels used in regions on the structure and the substrate, respectively, to calculate the phase-step curve. (d)–(e) Measured phase step between the structure and the substrate (black datapoints) and the theoretical solution fit (solid light green). In addition, shown are the curves calculated from the found solution with varied substrate SiO_2 thickness between 1.5 and 4.5 nm in a 0.25 nm increment in (d) and varied structure height between 18.0 and 22.5 nm in a 0.3 nm increment in (e).

change in contrast between the structure and the substrate among the images comes from the incidence-angle dependent change in the phase-upon-reflection of EUV light from the sample; the circular contrast change at the center is due to the slight buildup of EUV-induced carbon contamination.

The phase step between the SiO_2 structure and the substrate was calculated as the difference of the mean of the phase values of the pixels in the black and white rectangles shown in the 19° reconstruction of Fig. 5(b). This is shown as the black datapoints in Figs. 5(d) and 5(e).

The genetic algorithm solved for the thickness of the passive SiO_2 on the Si substrate and the topographic height of the SiO_2 structures. The solution found and the confidence intervals are reported in Table III. Both parameters are solved with sub-nanometer confidence intervals and are consistent with the estimate of the SiO_2 thickness (~2.5 nm) and the calibrated height (20.8 ± 0.4 nm) provided by the manufacturer. The sensitivities to the two solved parameters are also shown by the well-separated theoretical curves in Figs. 5(d) and 5(e) that are calculated from the solution but with individually varied parameter values.

TABLE III. Fitted parameters and confidence intervals of SiO_2 structures on a Si substrate measured by imaging reflectometry.

	Fitted parameters	Confidence interval	
		Multi-parameter	Single-parameter
Substrate SiO_2 thickness (nm)	3.0	0.6	<0.1
Structure height (nm)	20.1	0.8	<0.1

EUV imaging reflectometry is an extremely unique technique in that it can measure the composition and layer thickness on and around non-periodic nanostructures in a spatially resolved manner without destructive sample preparation or milling. This set of capabilities is not provided by many other commonly used metrology techniques. Furthermore, the ability to identify defects or impurities in the reconstruction and avoid them in the

09 July 2024 17:34:48

Published under an exclusive license by AIP Publishing

composition reconstruction is an advantage over traditional model-based techniques.

VI. CONCLUSION AND OUTLOOK

We have demonstrated the performance of a tabletop EUV reflectometer for imaging and characterization of nanostructures. We present measurements from three modes of reflectometry that are possible on this system, namely, intensity reflectometry, scatterometry, and coherent diffractive imaging reflectometry, each demonstrating the high sensitivity of EUV light to topography and composition.

The three modes of reflectometry each cater to different length scales and periodicities of nanostructures: intensity reflectometry for transversely uniform bulk and thin film geometry, scatterometry for periodic structures, and imaging reflectometry for non-periodic structures. While the demonstration of the three modes was conducted on different samples in this study, we note that it is possible to characterize a single sample with multiple modes for enhanced precision of measurement. For example, a sample with periodic structures may have a large portion of the substrate that is uncovered by structures, which can first be measured by intensity reflectometry. The solution can then assist in the modeling of the sample in scatterometry for a more precise characterization of the structures. In addition, while not described in this publication, the system can also be used to qualitatively characterize non-periodic nanoscale structures on the surface of a sample (such as nanoparticle size and distribution) from the shape and intensity of the EUV scatter pattern or simply operate as a ptychographic microscope by taking an image at a chosen incidence angle.

The ability to non-destructively measure the geometry and composition of nanostructures on a few to tens of μm^2 field of view with sub-nanometer precision is a combination of strengths unique to this EUV reflectometer and is largely unmatched by the existing array of commonly used metrology techniques. By realizing this special capability on a tabletop setup, the EUV reflectometer demonstrates the applicability of EUV metrology to a wide range of semiconductor and material science challenges. Finally, we note that in the future, imaging reflectometry could be used to locally characterize highly periodic samples by using structured EUV beams with orbital angular momentum that enhances the diversity in the collected scatter patterns.[61] In addition, by increasing the EUV flux (~100×) and also using faster readout CMOS cameras, the throughput of the instrument can be further improved.

SUPPLEMENTARY MATERIAL

See the supplementary material for (1) procedure for the calculation of confidence intervals of solved parameters; (2) data processing procedure for intensity reflectometry and scatterometry; (3) data pre-processing, ptychographic reconstruction, and image analysis procedure for imaging reflectometry; (4) ptychographically reconstructed probes in the imaging reflectometry demonstration; and (5) detailed sample model descriptions.

ACKNOWLEDGMENTS

This research was performed at JILA, University of Colorado. The authors acknowledge support from the STROBE National Science Foundation Science and Technology Center, Grant No. DMR-1548924. We also acknowledge support from Grant No. AWD-22-06-0106 from Samsung Telecommunications America, LLC, for the imaging reflectometry demonstration in this work and for suggesting the AFM calibration sample. The authors would like to thank Christina Porter as one of the initial co-designers of the reflectometer in 2016–2018 (JILA, University of Colorado Boulder); Weilun Chao (Lawrence Berkeley National Laboratory) for fabrication of the gold thin film sample; Samuel Marks (University of Colorado Boulder) for assisting the collection of x-ray reflectivity measurements on the gold thin film sample; J. Curtis Beimborn II and Amy Ekiriwang (JILA, University of Colorado Boulder) for assisting with other components fabrication and metrology; and Brendan McBennett and Joshua L. Knobloch (JILA, University of Colorado Boulder) for helpful discussions. J.M.S. fabricated the grating sample used in the scatterometry demonstration and performed correlative metrology. He is a member of the Quantum Electromagnetics Division of the National Institute of Standards and Technology (NIST). Certain commercial equipment, instruments, or materials are identified in this paper in order to adequately specify the experimental procedure. Such identification is not intended to imply recommendation or endorsement by NIST, nor is it intended to imply that the materials or equipment identified are necessarily the best available for the purpose.

AUTHOR DECLARATIONS

Conflict of Interest

H.C.K. and M.M.M. have a financial interest in KMLabs, which produced the laser source used in this work. H.C.K. is partially employed by KMLabs. M.M.M., H.C.K., and M.T. are inventors on a U.S. patent application (2021/0325301 A1, published October 21, 2021) and a patent in the European Patent Office (EP3458837B1) related to this work filed by the University of Colorado.

Author Contributions

Yuka Esashi: Conceptualization (supporting); Data curation (lead); Formal analysis (lead); Investigation (lead); Methodology (lead); Project administration (supporting); Software (supporting); Validation (lead); Visualization (lead); Writing – original draft (lead); Writing – review & editing (lead). **Nicholas W. Jenkins**: Conceptualization (supporting); Data curation (supporting); Formal analysis (supporting); Investigation (supporting); Methodology (supporting); Software (supporting); Validation (supporting); Writing – review & editing (supporting). **Yunzhe Shao**: Data curation (supporting); Formal analysis (supporting); Investigation (supporting); Validation (supporting); Writing – review & editing (supporting). **Justin M. Shaw**: Formal analysis (supporting); Resources (supporting). **Seungbeom Park**: Resources (supporting). **Margaret M. Murnane**: Conceptualization (lead); Funding acquisition (lead); Investigation (lead); Methodology (lead); Project administration (lead); Resources (lead); Supervision (lead); Validation (supporting); Writing – original draft (lead); Writing – review & editing (supporting). **Henry C. Kapteyn**: Conceptualization (lead); Funding acquisition (lead); Investigation (lead); Methodology (lead); Project administration (lead); Resources (lead); Supervision (lead); Writing – original draft (lead);

09 July 2024 17:34:48

Published under an exclusive license by AIP Publishing

Writing – review & editing (supporting). **Michael Tanksalvala**: Conceptualization (lead); Methodology (lead); Software (lead); Supervision (supporting); Validation (supporting); Visualization (supporting); Writing – original draft (lead); Writing – review & editing (supporting).

DATA AVAILABILITY

The data that support the findings of this study are available from the corresponding author upon reasonable request.

REFERENCES

[1] N. G. Orji, M. Badaroglu, B. M. Barnes, C. Beitia, B. D. Bunday, U. Celano, R. J. Kline, M. Neisser, Y. Obeng, and A. E. Vladar, "Metrology for the next generation of semiconductor devices," Nat. Electr. **1**, 532–547 (2018).
[2] G. Orji, B. Bunday, and Y. Obeng, *International Roadmap for Devices and Systems: Metrology* (IEEE, 2022).
[3] K. M. Hoogeboom-Pot, J. N. Hernandez-Charpak, X. Gu, T. D. Frazer, E. H. Anderson, W. Chao, R. W. Falcone, R. Yang, M. M. Murnane, H. C. Kapteyn, and D. Nardi, "A new regime of nanoscale thermal transport: Collective diffusion increases dissipation efficiency," Proc. Natl. Acad. Sci. U. S. A. **112**, 4846–4851 (2015).
[4] T. D. Frazer, J. L. Knobloch, J. N. Hernández-Charpak, K. M. Hoogeboom-Pot, D. Nardi, S. Yazdi, W. Chao, E. H. Anderson, M. K. Tripp, S. W. King, H. C. Kapteyn, M. M. Murnane, and B. Abad, "Full characterization of ultrathin 5-nm low-k dielectric bilayers: Influence of dopants and surfaces on the mechanical properties," Phys. Rev. Mater. **4**, 073603 (2020).
[5] J. Fontcuberta, H. B. Vasili, J. Gàzquez, and F. Casanova, "On the role of interfaces on spin transport in magnetic insulator/normal metal heterostructures," Adv. Mater. Interfaces **6**, 1900475 (2019).
[6] E. Gullikson, S. Mrowka, and B. Kaufmann, "Recent developments in EUV reflectometry at the advanced light source," in *Emerging Lithographic Technologies V*, (SPIE, 2001), Vol. 4343.
[7] F. Scholze, J. Tümmler, and G. Ulm, "High-accuracy radiometry in the EUV range at the PTB soft x-ray beamline," Metrologia **40**, S224–S228 (2003).
[8] C. Tarrio, S. Grantham, M. B. Squires, R. E. Vest, and T. B. Lucatorto, "Towards high accuracy reflectometry for extreme-ultraviolet lithography," J. Res. Natl. Inst. Stand. Technol. **108**, 267–273 (2003).
[9] S. Nannarone, F. Borgatti, A. DeLuisa, B. P. Doyle, G. C. Gazzadi, A. Giglia, P. Finetti, N. Mahne, L. Pasquali, M. Pedio, G. Selvaggi, G. Naletto, M. G. Pelizzo, and G. Tondello, "The BEAR beamline at elettra," AIP Conf. Proc. **705**, 450–453 (2004).
[10] H. Iguchi, H. Hashimoto, M. Kuki, T. Harada, H. Kinoshita, T. Watanabe, Y. Y. Platonov, M. D. Kriese, and J. R. Rodriguez, "Extreme-ultraviolet collector mirror measurement using large reflectometer at NewSUBARU synchrotron facility," Jpn. J. Appl. Phys. **55**, 06GC01 (2016).
[11] E. M. Gullikson, J. H. Underwood, P. C. Batson, and V. Nikitin, "A soft X-ray/EUV reflectometer based on a laser produced plasma source," J. X-Ray Sci. Technol. **3**, 283–299 (1992).
[12] D. L. Windt and W. K. Waskiewicz, "Soft X-ray reflectometry of multilayer coatings using a laser-plasma source," in *Multilayer Optics for Advanced X-Ray Applications* (SPIE, 1991), Vol. 1547.
[13] M. Banyay and L. Juschkin, "Table-top reflectometer in the extreme ultraviolet for surface sensitive analysis," Appl. Phys. Lett. **94**, 063507 (2009).
[14] S. Döring, F. Hertlein, A. Bayer, and K. Mann, "EUV reflectometry for thickness and density determination of thin film coatings," Appl. Phys. A **107**, 795–800 (2012).
[15] J. J. Abel, F. Wiesner, J. Nathanael, J. Reinhard, M. Wünsche, G. Schmidl, A. Gawlik, U. Hübner, J. Plentz, C. Rödel, G. G. Paulus, and S. Fuchs, "Absolute EUV reflectivity measurements using a broadband high-harmonic source and an in situ single exposure reference scheme," Opt. Express **30**, 35671–35683 (2022).
[16] J. Perlich, F.-M. Kamm, J. Rau, F. Scholze, and G. Ulm, "Characterization of extreme ultraviolet masks by extreme ultraviolet scatterometry," J. Vac. Sci. Technol., B: Microelectron. Nanometer Struct.–Process., Meas., Phenom. **22**, 3059–3062 (2004).
[17] F. Scholze, C. Laubis, U. Dersch, J. Pomplun, S. Burger, and F. Schmidt, "Influence of line edge roughness and CD uniformity on EUV scatterometry for CD characterization of EUV masks," in *Modeling Aspects in Optical Metrology* (SPIE, 2007), Vol. 6617, pp. 400–409.
[18] H. Gross, A. Rathsfeld, F. Scholze, and M. Bär, "Profile reconstruction in extreme ultraviolet (EUV) scatterometry: Modeling and uncertainty estimates," Meas. Sci. Technol. **20**, 105102 (2009).
[19] M.-A. Henn, S. Heidenreich, H. Gross, A. Rathsfeld, F. Scholze, and M. Bär, "Improved grating reconstruction by determination of line roughness in extreme ultraviolet scatterometry," Opt. Lett. **37**, 5229–5231 (2012).
[20] Y.-S. Ku, C.-L. Yeh, Y.-C. Chen, C.-W. Lo, W.-T. Wang, and M.-C. Chen, "EUV scatterometer with a high-harmonic-generation EUV source," Opt. Express **24**, 28014 (2016).
[21] L. Bahrenberg, S. Danylyuk, S. Glabisch, M. Ghafoori, S. Schröder, S. Brose, J. Stollenwerk, and P. Loosen, "Characterization of nanoscale gratings by spectroscopic reflectometry in the extreme ultraviolet with a stand-alone setup," Opt. Express **28**, 20489 (2020).
[22] A. Fernández Herrero, F. Scholze, G. Dai, and V. Soltwisch, "Analysis of line-edge roughness using EUV scatterometry," Nanomanuf. Metrol. **5**, 149–158 (2022).
[23] L. M. Lohr, R. Ciesielski, S. Glabisch, S. Schröder, S. Brose, and V. Soltwisch, "Nanoscale grating characterization using EUV scatterometry and soft x-ray scattering with plasma and synchrotron radiation," Appl. Opt. **62**, 117–132 (2023).
[24] C. Porter, T. Coenen, N. Geypen, S. Scholz, L. van Rijswijk, H.-K. Nienhuys, J. Ploegmakers, J. Reinink, H. Cramer, R. van Laarhoven, D. O'Dwyer, P. Smorenburg, A. Invernizzi, R. Wohrwag, H. Jonquiere, J. Reinhardt, O. el Gawhary, S. Mathijssen, P. Engblom, H. Chin, W. T. Blanton, S. Ganesan, B. Krist, F. Gstrein, and M. Phillips, "Soft x-ray: Novel metrology for 3D profilometry and device pitch overlay," in *Metrology, Inspection, and Process Control XXXVII* (SPIE, 2023), Vol. 12496, pp. 412–420.
[25] M. Tanksalvala, C. L. Porter, Y. Esashi, B. Wang, N. W. Jenkins, Z. Zhang, G. P. Miley, J. L. Knobloch, B. McBennett, N. Horiguchi, S. Yazdi, J. Zhou, M. N. Jacobs, C. S. Bevis, R. M. Karl Jr., P. Johnsen, D. Ren, L. Waller, D. E. Adams, S. L. Cousin, C.-T. Liao, J. Miao, M. Gerrity, H. C. Kapteyn, and M. M. Murnane, "Nondestructive, high-resolution, chemically specific 3D nanostructure characterization using phase-sensitive EUV imaging reflectometry," Sci. Adv. **7**, eabd9667 (2021).
[26] E. Chason and T. M. Mayer, "Thin film and surface characterization by specular X-ray reflectivity," Crit. Rev. Solid State Mater. Sci. **22**, 1–67 (1997).
[27] K. N. Stoev and K. Sakurai, "Review on grazing incidence X-ray spectrometry and reflectometry," Spectrochim. Acta, Part B **54**, 41–82 (1999).
[28] G. Freychet, D. Kumar, R. Pandolfi, D. Staacks, P. Naulleau, R. J. Kline, D. Sunday, M. Fukuto, J. Strzalka, and A. Hexemer, "Critical-dimension grazing incidence small angle x-ray scattering," *Metrology, Inspection, and Process Control for Microlithography XXXII* (SPIE, 2018), Vol. 10585, pp. 217–223.
[29] W. Wu, R. Joseph Kline, R. L. Jones, H.-J. Lee, E. K. Lin, D. F. Sunday, C. Wang, T. Hu, and C. L. Soles, "Review of the key milestones in the development of critical dimension small angle x-ray scattering at National Institute of Standards and Technology," J. Micro/Nanopatterning, Mater., Metrol. **22**, 031206 (2023).
[30] D. Attwood and A. Sakdinawat, Scattering, diffraction, and refraction of electromagnetic radiation, *X-Rays and Extreme Ultraviolet Radiation* (Springer, 2016), pp. 20–24.
[31] B. L. Henke *et al.*, "X-ray interactions: Photoabsorption, scattering, transmission, and reflection at E = 50-30,000 eV, Z = 1-92," At. Data Nucl. Data Tables **54**, 181–342 (1993).
[32] C. T. Chantler, "Detailed tabulation of atomic form factors, photoelectric absorption and scattering cross section, and mass attenuation coefficients in the vicinity of absorption edges in the soft X-ray (Z = 30–36, Z = 60–89, E = 0.1 keV–10 keV), addressing convergence issues of earlier work," J. Phys. Chem. Ref. Data **29**, 597–1056 (2000).

09 July 2024 17:34:48

Published under an exclusive license by AIP Publishing

[33] L. G. Parratt, "Surface studies of solids by total reflection of X-rays," Phys. Rev. **95**, 359–369 (1954).
[34] L. Névot and P. Croce, "Caractérisation des surfaces par réflexion rasante de rayons X. Application à l'étude du polissage de quelques verres silicates," Rev. Phys. Appl. **15**, 761–779 (1980).
[35] Y. Esashi, M. Tanksalvala, Z. Zhang, N. W. Jenkins, H. C. Kapteyn, and M. M. Murnane, "Influence of surface and interface roughness on X-ray and extreme ultraviolet reflectance: A comparative numerical study," OSA Continuum **4**, 1497–1518 (2021).
[36] M. G. Moharam and T. K. Gaylord, "Rigorous coupled-wave analysis of planar-grating diffraction," J. Opt. Soc. Am. **71**, 811–818 (1981).
[37] M. G. Moharam, E. B. Grann, D. A. Pommet, and T. K. Gaylord, "Formulation for stable and efficient implementation of the rigorous coupled-wave analysis of binary gratings," J. Opt. Soc. A. A **12**, 1068–1076 (1995).
[38] J. T. Hollenshead, L. E. Klebanoff, and G. Delgado, "Predicting radiation-induced carbon contamination of EUV optics," J. Vac. Sci. Technol., B: Nanotechnol. Microelectron.: Mater., Process., Meas., Phenom. **37**, 021602 (2019).
[39] A. D. Dane, A. Veldhuis, D. Boer, A. J. G. Leenaers, and L. Buydens, "Application of genetic algorithms for characterization of thin layered materials by glancing incidence X-ray reflectometry," Physica B **253**, 254–268 (1998).
[40] A. Ulyanenkov, K. Omote, and J. Harada, "The genetic algorithm: Refinement of X-ray reflectivity data from multilayers and thin films," Physica B **283**, 237–241 (2000).
[41] W. H. Press, S. A. Teukosky, W. T. Vetterling, and B. P. Flannery, Modeling of data, *Numerical Recipes: The Art of Scientific Computing*, 3rd ed. (Cambridge University Press, 2007), pp. 773–839.
[42] W. Fischer, H. Geiger, P. Rudolf, and P. Wissmann, "Structure investigations on single-crystal gold films," Appl. Phys. **13**, 245–253 (1977).
[43] J. Siegel, O. Lyutakov, V. Rybka, Z. Kolská, and V. Švorčík, "Properties of gold nanostructures sputtered on glass," Nanoscale Res. Lett. **6**, 96 (2011).
[44] A. Kato and F. Scholze, "Effect of line roughness on the diffraction intensities in angular resolved scatterometry," Appl. Opt. **49**, 6102–6110 (2010).
[45] A. Fernández Herrero, M. Pflüger, J. Probst, F. Scholze, and V. Soltwisch, "Applicability of the Debye-Waller damping factor for the determination of the line-edge roughness of lamellar gratings," Opt. Express **27**, 32490–32507 (2019).
[46] D. Sayre, "Some implications of a theorem due to Shannon," Acta Crystallogr. **5**, 843 (1952).
[47] J. M. Rodenburg and H. M. L. Faulkner, "A phase retrieval algorithm for shifting illumination," Appl. Phys. Lett. **85**, 4795–4797 (2004).
[48] A. M. Maiden and J. M. Rodenburg, "An improved ptychographical phase retrieval algorithm for diffractive imaging," Ultramicroscopy **109**, 1256–1262 (2009).
[49] P. Thibault, M. Dierolf, O. Bunk, A. Menzel, and F. Pfeiffer, "Probe retrieval in ptychographic coherent diffractive imaging," Ultramicroscopy **109**, 338–343 (2009).
[50] J. Miao, R. L. Sandberg, and C. Song, "Coherent X-ray diffraction imaging," IEEE J. Sel. Top. Quantum Electron. **18**, 399–410 (2012).
[51] J. Miao, T. Ishikawa, I. K. Robinson, and M. M. Murnane, "Beyond crystallography: Diffractive imaging using coherent x-ray light sources," Science **348**, 530–535 (2015).
[52] F. Pfeiffer, "X-ray ptychography," Nat. Photonics **12**, 9–17 (2018).
[53] L. Loetgering, S. Witte, and J. Rothhardt, "Advances in laboratory-scale ptychography using high harmonic sources [Invited]," Opt. Express **30**, 4133–4164 (2022).
[54] E. R. Shanblatt, C. L. Porter, D. F. Gardner, G. F. Mancini, R. M. Karl, M. D. Tanksalvala, C. S. Bevis, V. H. Vartanian, H. C. Kapteyn, D. E. Adams, and M. M. Murnane, "Quantitative chemically specific coherent diffractive imaging of reactions at buried interfaces with few nanometer precision," Nano Lett. **16**, 5444–5450 (2016).
[55] D. F. Gardner, M. Tanksalvala, E. R. Shanblatt, X. Zhang, B. R. Galloway, C. L. Porter, R. Karl Jr, C. Bevis, D. E. Adams, H. C. Kapteyn, M. M. Murnane, and G. F. Mancini, "Subwavelength coherent imaging of periodic samples using a 13.5 nm tabletop high-harmonic light source," Nat. Photonics **11**, 259–263 (2017).
[56] A. Maiden, D. Johnson, and P. Li, "Further improvements to the ptychographical iterative engine," Optica **4**, 736–745 (2017).
[57] P. Thibault and A. Menzel, "Reconstructing state mixtures from diffraction measurements," Nature **494**, 68–71 (2013).
[58] D. J. Batey, D. Claus, and J. M. Rodenburg, "Information multiplexing in ptychography," Ultramicroscopy **138**, 13–21 (2014).
[59] A. Beck and M. Teboulle, "Fast gradient-based algorithms for constrained total variation image denoising and deblurring problems," IEEE Trans. Image Process. **18**, 2419–2434 (2009).
[60] C. L. Porter, M. Tanksalvala, M. Gerrity, G. Miley, X. Zhang, C. Bevis, E. Shanblatt, R. Karl, M. M. Murnane, D. E. Adams, and H. C. Kapteyn, "General-purpose, wide field-of-view reflection imaging with a tabletop 13 nm light source," Optica **4**, 1552–1557 (2017).
[61] B. Wang, N. J. Brooks, P. Johnsen, N. W. Jenkins, Y. Esashi, I. Binnie, M. Tanksalvala, H. C. Kapteyn, and M. M. Murnane, "High-fidelity ptychographic imaging of highly periodic structures enabled by vortex high harmonic beams," Optica **10**, 1245–1252 (2023).

09 July 2024 17:34:48

Published under an exclusive license by AIP Publishing